Applied Clay Science 213 (2021) 106251

Contents lists available at ScienceDirect

Applied Clay Science

journal homepage: www.elsevier.com/locate/clay

Local Environments in Iron-Bearing Clay Minerals by DFT Approaches: The Case of Structural Fe in Kaolinite

Diego Richard [a,b,*], Nicolás Maximiliano Rendtorff [a,b]

[a] CETMIC, Centro de Tecnología de Recursos Minerales y Cerámica (CONICET La Plata - CIC PBA - UNLP), Camino Centenario y 506, C.C. 49, (B1897ZCA), M. B. Gonnet, Buenos Aires, Argentina
[b] Facultad de Ciencias Exactas, Universidad Nacional de La Plata, 47 y 115, La Plata, Buenos Aires, Argentina

ARTICLE INFO

Keywords:
DFT
Kaolinite
Mössbauer
iron-doped materials
Clay
electron transfer

ABSTRACT

Technological properties of kaolins depend on the internal structure of the particles that constitute them. For this reason, unraveling the structural features from the micro to the nanoscale is a permanent matter of interest, even in the case of raw samples. From the experimental point of view, because naturally-occurring kaolins contain iron, Mössbauer spectroscopy is a very convenient technique to reach the nanoscopic scale avoiding experimental difficulties related to the sample's lack of structural order at the crystallographic scale.

In this work, first-principles calculations based on the Density Functional Theory (DFT) were used to model such iron environments in kaolinite, and to assess the performance of the Gauge-Included Projector Augmented Waves (GIPAW) method to describe the changes to the host structure and the electronic modifications produced by the iron atoms. To this purpose, structural relaxation, Grimme's D2 dispersion, and Hubbard corrections (DFT+*U* approach) were considered. A detailed analysis was done for the obtained predictions for the Fe local structure, oxidation state, and Mössbauer quadrupole splitting, including comparisons with available experimental data. The results contribute to better understand the naturally-occurring kaolins, and support the DFT+*U* approach for the description of the layer structure and the electronic properties of iron-containing clay minerals.

1. Introduction

Iron-bearing clay minerals are ubiquitous in soil, and are important redox agents in the subsurface as they contain structural iron in both Fe^{II} and Fe^{III} forms. Because they can act as both electron donors and acceptors through the reactive Fe, they impact in a wide variety of geochemical processes (Soltermann et al., 2013; Latta et al., 2017). Among the clay minerals, kaolins are extensively used in the industry because of their many technological applications, which include ceramics, cement, refractories, pharmaceuticals, paper, and plastics, among many others (Schroeder and Erickson, 2014). The clay technological performance may depend on the internal structural modifications produced during its processing, where the presence of impurities and the thermal treatments conducted are important conditions (Chakraborty, 2014). In this way, the study of the dehydroxylation reaction of kaolinite and the establishment of realistic models are current challenges in this area, due to the complexity of the structural modifications that appear during the kaolin-metakaolin (K-MK) transition (Kloprogge, 2019). In the last years, different experimental strategies have been used to analyze the changes in the structural order and the formation of intermediate phases during the dehydroxylation process (Gasparini et al., 2013; White et al., 2013; Andrini et al., 2016; Drits et al., 2016; Gadikota et al., 2017; Yan and Wang, 2018; Conconi et al., 2019; Drits et al., 2019; Daou et al., 2020). Among them, it is common to find studies that involve NMR, XANES, and Mössbauer spectroscopies applied to kaolinites (Fabbri et al., 2013; Lin et al., 2013; Andrini et al., 2016; Gadikota et al., 2017; Danner et al., 2018). These techniques allow accessing the sample structure locally (at the sub-crystallographic scale), and avoid typical experimental difficulties related to the lack of structural order, which are typical in MK. Then, these techniques emerge as very appropriate to sense the local structures and gain insight during clay processing. In particular, ^{57}Fe Mössbauer spectroscopy is a perfect tool to study raw kaolins, considering that Fe is known to occur in them as the main impurity into the kaolinite host lattice and also in the accessory clay minerals. Investigations have used the high sensitivity of the Mössbauer spectroscopy to learn about the local environments of

* Corresponding author at: CETMIC, Centro de Tecnología de Recursos Minerales y Cerámica (CONICET La Plata - CIC PBA - UNLP), Camino Centenario y 506, C.C. 49, (B1897ZCA), M. B. Gonnet, Buenos Aires, Argentina.
E-mail address: richard@fisica.unlp.edu.ar (D. Richard).

https://doi.org/10.1016/j.clay.2021.106251
Received 11 May 2021; Received in revised form 6 August 2021; Accepted 13 August 2021
Available online 19 August 2021

iron in kaolins, and also as a tool to study the materials through properties that depend on the structural Fe vicinity (St. Pierre et al., 1992; Castelein et al., 2002; Hart et al., 2002; Soro et al., 2003; Sei et al., 2004; Scorzelli et al., 2008; Andji et al., 2009; Silva et al., 2009; Santos et al., 2012; Zalutskii, 2014; Gonçalves et al., 2020). Mössbauer spectroscopy allows the determination of the isomer shift (IS) and the quadrupole splitting (QS). The IS is sensitive to the oxidation state of iron, and can provide information on the Fe coordination, whereas the QS provides a measure of the Fe site distortion (Murad, 2010). The QS arises from the interaction of the electric quadrupole moment of the Fe nucleus with its surrounding electric field gradient (EFG), which is extremely sensitive to changes in the symmetry of the electronic charge density close to the Fe nucleus (due to its r^{-3} dependence from the charge sources). Mössbauer results in kaolins indicate that samples from different sources present trivalent iron (Fe^{III}) and, in many cases, a lower amount of divalent iron (Fe^{II}), both in the high-spin state and in octahedral coordination. These observed iron coordinations indicate that Fe atoms occur as isomorphic substitutions of Al atoms in the octahedral sheet, with very different values of QS for the high-spin Fe^{III} and Fe^{II} contributions (about 0.5 mm/s and 2.5 mm/s, respectively) (Murad, 2010). Because it occurs in two oxidation states which are easily distinguished with Mössbauer spectroscopy, this structural Fe can be used as an indicator of the nature of the clay mineral and other geochemical features, such as the changes in oxidizing properties during chemical and thermal treatments (Gualtieri et al., 2000; Wagner and Wagner, 2004; Rivard et al., 2013; Zhu et al., 2019). Yet, there is still much work to do in order to sketch effective models that account for the amorphous phases that appear in raw kaolinites after the subsequent treatments (Provis et al., 2009).

In regard to theoretical studies, first-principles calculations based on the Density Functional Theory (DFT) have become very useful tools to model kaolinites and other related clay minerals. In the last decade, DFT-based methods were successfully used to investigate different properties of defect-free kaolinites (Mercier and Le Page, 2008; Zhou et al., 2009; Smrcok et al., 2010; Paris, 2014) and also kaolinite with defects (vacancies and impurities) (He et al., 2009; Nisar et al., 2011; Johnson and Otero-de-la-Roza, 2012; Pietzsch et al., 2015; Fu and Yang, 2017; Zhao et al., 2020). In particular, DFT modeling aided to reconcile discrepancies regarding the exact geometry of the kaolinite layer structure (White et al., 2009; Richard and Rendtorff, 2019). However, the most conventional DFT functionals are not accurate enough for some physical situations: they usually fail in the description of weak nonbonding interactions (such as hydrogen bonding) and, when Fe is present in the system, they are known to underestimate the Coulomb repulsion between the delocalized 3*d*-electrons. Therefore, the current state-of-the-art of *ab initio* methods indicates that depending on the considered clay mineral system different corrections must be included. In this sense, it has been shown that dispersion corrections may play a significant role in the correct description of the structural parameters in phyllosilicates (Tunega et al., 2012) and, for Fe-bearing clay minerals, an accurate description of the 3*d*-electrons of Fe generally requires the use of Hubbard corrections (the so-called DFT+U method) (Geatches et al., 2013; Kéri et al., 2017, 2020). On the other hand, DFT-based methods have been shown an overall good performance for predicting Mössbauer parameters in many different structures (Bochevarov et al., 2010; Pápai and Vankó, 2013; Zyabkin et al., 2020; Mudarra Navarro et al., 2021). Then, considering all this experimental and theoretical background, it becomes relevant to assess the DFT methods for predicting structural Fe local environments in kaolinite. In particular, accurate predictions for the QS values in Fe-doped kaolinites can provide alternative and valuable approaches for describing such systems, which would complement the experimental data, and help to obtain more reliable methods to model clay materials at this level.

This work presents a study of the Fe-doped kaolinite using the gauge-including projector augmented wave (GIPAW) method (Pickard and Mauri, 2001; Profeta et al., 2003). GIPAW has been mostly used for predicting the EFG and other hyperfine properties in minerals and ceramics (Apaolaza et al., 2020; Charpentier, 2011) and, most recently, in pure kaolinite (Richard and Rendtorff, 2019) and doped compounds (Richard and Gil Rebaza, 2020; Rocha-Rodrigues et al., 2020). The aim of this work is to extend such investigations to the case of Fe-doped kaolinite, by doing a comprehensive analysis of the current DFT approaches for predicting the Fe^{III} and Fe^{II} local environments in the kaolinite bulk structure, and relate them with the electronic structure of the clay mineral. To this purpose, Fe atoms were substitutionally introduced at Al sites of the kaolinite host structure, and different calculation approaches were assessed for predicting the QS values. Results from calculations on this clay mineral using GIPAW can be used to improve models in other iron-bearing clay minerals, which are of importance to unravel both the geochemical processes related to the presence of the Fe redox buffer, and the clay technological performance in their industrial applications.

2. Methodology

The kaolinite starting structure in this investigation corresponds to that of the theoretical defect-free kaolinite calculated in a recent investigation with the GIPAW method (Fig. 1). This structure was used as the clay mineral host lattice, in which an Fe atom is introduced as a bulk impurity, replacing one Al atom in the 34-atom unit cell. The resulting doping amount is similar to that considered in recent studies for other heavy doped-kaolinites (Fu and Yang, 2017; Zhao et al., 2020).

DFT calculations were performed using the open-source Quantum ESPRESSO (QE) package, based on pseudopotentials and plane waves (Giannozzi et al., 2017). The DFT-D2 and DFT-D2+U approaches were considered to account for the electron correlations in the system. The role of the structural relaxations after Fe inclusion were evaluated. To this purpose, the initial structure input (non-relaxed structure) was optimized until forces in all atoms were below 0.025 eV/Å (relaxed structure). Also, three charge states were considered for the doped kaolinite system: that neutral, obtained after the substitution of the Al atom by the Fe atom (total charge = 0 in QE), and the other two after adding or subtracting one electron to the unit cell after substitution (total charge −1 and +1, respectively). Further details about the calculation procedure can be found in the supplementary material.

Because the kaolinite structure has two similar but inequivalent Al sites, the substitution leads to two possibilities: Fe at Al1 or Al2 sites (see Fig. 1), which are called Kaol-Fe1 and Kaol-Fe2 systems, respectively. From the analysis of the energy difference between Kaol-Fe1 and Kaol-Fe2, it was found an Fe occupation preference for Al2 site over Al1 (see Fig. S2 in the supplementary material). Therefore, in the following the Kaol-Fe2 case will be considered.

Finally, the GIPAW method was used for predicting the EFG tensor at

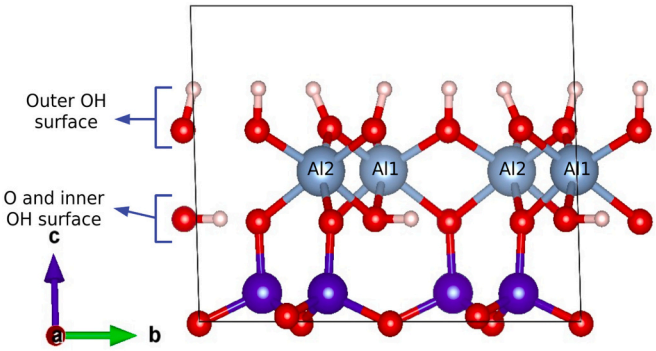

Fig. 1. Kaolinite unit cell, representation of the structure obtained using the atomic coordinates reported in Richard and Rendtorff (2019). The white, red, light blue, and blue spheres stand for H, O, Al, and Si atoms, respectively. (For interpretation of the references to colour in this figure legend, the reader is referred to the web version of this article.)

the Fe site in each obtained doped kaolinite structure. From this EFG, the Mössbauer QS was calculated as described in the supplementary material. This procedure allows the assessment of the predicted Fe local environments through the comparison of the calculated QS with those QS values determined in Mössbauer experiments.

3. Results

3.1. Electronic properties

The density of electronic states (DOS) of the undoped kaolinite has a forbidden energy band gap of about 5 eV (see Fig. S1). This value is in agreement with other reported theoretical data (Nisar et al., 2011; Fu and Yang, 2017; Richard and Rendtorff, 2019), but it is known that real kaolinites present multiple structural defects which vastly changes the electronic structure, introducing different defect states in the band gap (Pietzsch et al., 2015). In the case of Fe-doped kaolinite, after substituting an Al atom by the Fe atom, impurity levels appear in the band gap in the form of narrow bands. These levels may favor electron transfer and hence improve the reactivity of kaolinite (Chen et al., 2020).

In Fig. 2 are presented the spin-resolved DOS for the different charge states after structural relaxations in Kaol-Fe2. Spin-polarized calculations predict a small band gap between the impurity levels, even for the neutral system (charge state 0). On the left side of Fig. 2, it can be seen how the total DOS changes from one charge state to another. In particular, the electron subtractions from charge state −1 to +1 make the Fermi level E_F shift from near the conduction band minimum to near the valence band maximum, and modify the kaolinite semiconductor character from n-type to p-type. On the right side of Fig. 2, there is a

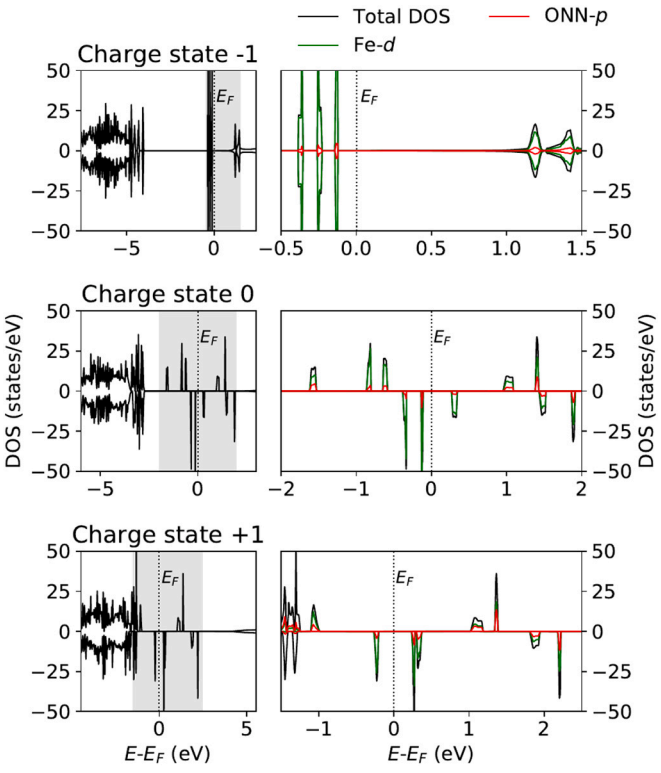

Fig. 2. Spin-resolved DOS calculated with the DFT method in the Kaol-Fe2 relaxed structure. On the left side is the total DOS corresponding to the different charge states, and the gray areas indicate the segments that are zoomed-in and showed in detail on the right side, together with Fe-*d* and ONN-*p* orbital partial DOS. Positive (negative) DOS is for spin-up (spin-down) states. For each DOS energies are referred to the Fermi energy E_F, also indicated with dotted vertical lines.

detail of the impurity levels near E_F, including the projected density of states (PDOS) of the iron *d* orbitals and its six oxygen nearest neighbors (ONN). These PDOS show that impurity levels are mainly composed by Fe-3*d* orbitals, and there is also a minor contribution to these levels from the ONN to the Fe impurity, which implies that it is a slightly covalent component in Fe—O bonds.

The unbalanced occupation of the spin-up and spin-down impurity levels (unpaired electrons) produces a total magnetization of 0, 1 and 2 μ_B per cell for the charge states −1, 0, and +1, respectively. Assuming a $3d^5$ configuration for Fe^{III}, these magnetization values indicate that DFT predicts the low-spin states of the different Fe oxidation states, and not the experimentally observed high-spin states corresponding to Fe^{III} and Fe^{II}. According to the PDOS of Fig. 2, the *d* orbitals of the iron impurity are splitted by the crystalline field in the material, and their occupation depends on the charge state of the system. Similar descriptions for these levels have been reported in the literature, in terms of t_{2g} and e_g-like orbitals (Fu and Yang, 2017; Ferreira et al., 2019) or, alternatively, using the HOMO-LUMO nomenclature for their occupation (Chen et al., 2020).

When the D2 correction is considered (DFT-D2 approach), minor changes appear in the calculated DOS, but they do not substantially modify the electronic character of the Kaol-Fe2 system from that observed in Fig. 2. Those DOS are provided in the supplementary material for further analysis (see Fig. S3). On the contrary, the addition of the *U* parameter in the DFT-D2+*U* approach produces a larger gap between Fe-3*d* occupied and unoccupied levels: the occupied 3*d* states are shifted well below the Fermi energy, and the unoccupied are pushed to higher energies, so their separation is about *U*. Therefore, this *ad-hoc* Coulomb correction could be added to tune the electronic band gap. Fig. S4 in the supplementary material is provided to show how higher *U* values produce higher band gaps. As a consequence, the number of unpaired electrons may be changed when this correction is applied, modifying the total magnetization of the system. In this sense, it was found that for *U* equal to or larger than 4 eV the magnetization for system charge states −1, 0, and +1 are 4, 5, and 4 μ_B per cell, respectively. These results are in much better agreement with those expected for high-spin states of Fe: the first two values (charge states −1 and 0) are equal to the magnetization corresponding to Fe^{II} and Fe^{III} (4 and 5 μ_B). In other words, the *U* correction can switch the low-spin to high-spin state and make the charge states −1 and 0 to be in agreement with the experimentally observed high-spin states of Fe^{II} and Fe^{III}, respectively (Murad, 1998; Hart et al., 2002; Murad, 2010).

In Fig. 3 are presented the DOS for Kaol-Fe2 using the DFT-D2+*U* approach with $U = 4$ eV. As can be seen, in comparison to the DOS obtained with the DFT method (those of Fig. 2), the correction produces an asymmetrical shifting of the spin-up and spin-down levels. This causes the change of the total magnetization. Taking into account the agreement with the experimental spin states obtained when considering the charge states −1 and 0, in the following, a more in-depth analysis will be performed for these two charge states.

3.2. Iron local environments

The isomorphic substitution of Al atoms by Fe produces a condition of non-equilibrium in the local structure that, after structural relaxations, leads to changes in the octahedral environments. In Table 1 are summarized parameters of the iron octahedral environments obtained with the DFT and DFT-D2+*U* approaches. As can be seen, after relaxations the octahedron volume *V* and the average Fe—O distances are increased in comparison to the starting non-relaxed structure. The highest changes are produced when the Hubbard correction is included: for charge state 0 the Fe—O distances are increased about 6%, and for charge state −1 these distances practically duplicate their increments. These results are in agreement with estimations using tabulated ionic radii. In this sense, the sum of the ionic radii of Al^{3+} and O^{2-} with coordinations 6 and 3, gives 1.895 Å. This value is slightly lower than the sum of the ionic radii corresponding to high-spin Fe^{3+} and O^{2-} (2.005

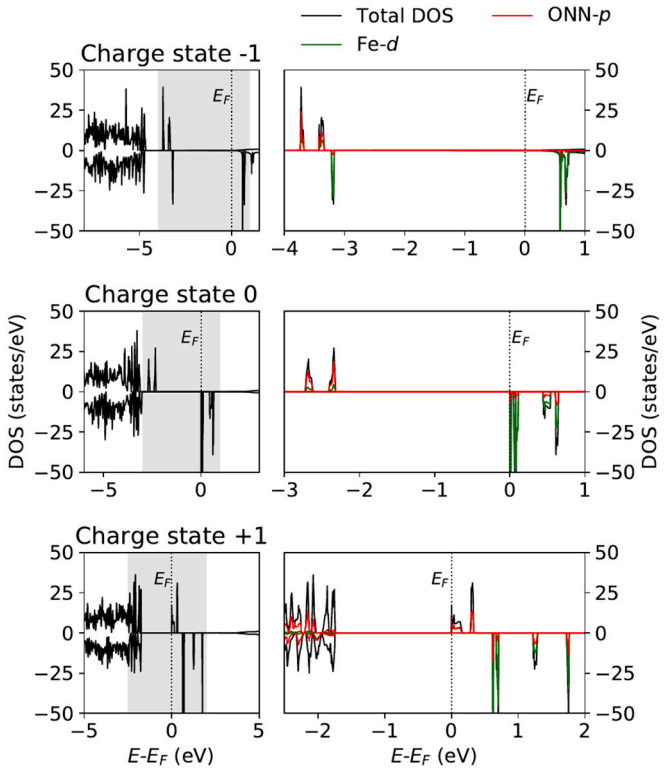

Fig. 3. Spin-resolved DOS calculated with the DFT-D2+U method (U = 4 eV) method in the Kaol-Fe2 relaxed structure. On the left side is the total DOS corresponding to the different charge states, and the gray areas indicate the segments that are zoomed-in and showed in detail on the right side, together with Fe-d and ONN-p orbital partial DOS. Positive (negative) DOS is for spin-up (spin-down) states. For each DOS energies are referred to the Fermi energy E_F, also indicated with dotted vertical lines.

Table 1
Iron octahedral environment parameters obtained using DFT and DFT-D2+U approaches for the charge states 0 and − 1 (indicated in parenthesis): octahedron volume V, average distance <Fe-O>, distortion parameters ζ, Δ, Σ, and Θ, distance H between the octahedron faces at the inner and outer surfaces, distance h from Fe atom to the face at the outer surface, and h/H ratio.

	Non-relaxed	DFT (0)	DFT (−1)	DFT-D2+U (0)	DFT-D2+U (−1)
V (Å^3)	9.039	9.281	10.322	10.770	12.383
<Fe-O> (Å)	1.912	1.926	1.999	2.028	2.134
ζ (Å)	0.320	0.264	0.222	0.334	0.276
Δ ($\times 10^{-4}$)	9.6	6.2	4.4	9.1	5.8
Σ (°)	82.64	79.56	82.86	82.99	94.20
Θ (°)	254.35	249.88	258.02	263.77	292.98
H (Å)	2.057	2.022	2.014	2.130	2.199
h (Å)	0.922	0.969	1.000	0.938	0.979
h/H	0.45	0.48	0.50	0.44	0.45

Å), and those of high-spin Fe^{2+} and O^{2-} (2.140 Å) (Shannon, 1976); *i. e.* compared to Al—O bond lengths, Fe^{3+}-O^{2-} and Fe^{2+}-O^{2-} present percentage increases of 6% and 12%, respectively. These incremental changes are in excellent agreement with the results obtained with the DFT-D2+U approach (see Table 1). The larger Fe—O distances compared to those of Al—O have been also predicted by first-principles calculations in the work of Fu and Yang (2017), as well as XRD measurements have suggested slight increments in the lattice parameters where the iron impurities are present (Petit and Decarreau, 1990; Soro et al., 2003; Zhu et al., 2019).

Table 1 also presents the octahedral distortion parameters: distance distortion ζ (sum of the deviation from the average Fe—O distance), tilting distortion Δ (mean quadratic Fe—O elongation), angle distortion Σ (sum of the deviation of the cis angles from right angle), and torsional distortion Θ (sum of the deviation of the angles between two vectors of two twisting face from 60°) (Ketkaew et al., 2019). In general, the obtained ζ parameters are slightly smaller than that corresponding to the starting non-relaxed structure, showing that after structural relaxations the Fe—O distances tend to be less dispersed around the mean. This is also reflected by the differences in Δ. On the other hand, the behavior of Σ and Θ depends on the considered approach. For DFT, both Σ and Θ are near the corresponding values to the non-relaxed structure, or slightly decrease, which indicates that the octahedral site maintains similar distortion. By contrast, DFT-D2+U predicts higher values for Σ and Θ, which indicates higher deviations in the Fe—O_6 geometry from the perfect octahedron.

Finally, Table 1 presents the distance H between the octahedron faces at the inner and outer surfaces (see Fig. 1), the distance h from the Fe atom to the octahedron face at the outer surface, and the h/H ratio. These parameters serve to estimate the iron octahedron disposal near the kaolinite layer outer surface. As can be seen, the H values do not follow the same increase as Fe—O distances: for DFT predictions H is nearly constant, and for DFT-D2+U it is increased up to about 7% for charge state −1. This indicates that after relaxation the octahedron presents a slight flattening in the [001] direction. The h/H ratio shows that in DFT calculations the Fe atoms are located practically at the center of the octahedron, while DFT-D2+U predicts a slight displacement towards the outer surface, which means that Fe—O bonds at the layer outer surface side are shorter than those of the internal Si tetrahedral sheet side. The predicted octahedral features in Table 1 indicate that the high-spin description obtained through the inclusion of the U correction is also accompanied by changes in the iron vicinity that are consistent with ionic radii data. In the supplementary material, Fig. S5 helps to visualize the subtle structural changes obtained after relaxation. In addition, the atomic positions for all the calculated structures are provided for further analysis, and also complete tables with the octahedral parameters corresponding to the DFT-D2 approach (which in general presents similar structural features to those obtained with DFT) and the charge state +1 (see Tables S1-S3).

In order to show the charge distribution around the Fe atom, in Fig. 4 are presented the results of the electronic charge ρ *via* the integration of local density of states (ILDOS). Based on the good description of the system using DFT-D2+U approach, it was considered this method to represent the spatial distribution of ρ for the DOS representative energy ranges. Fig. 4a shows that the main contribution to the valence band is due to oxygen atoms, as observed through the DOS of the undoped

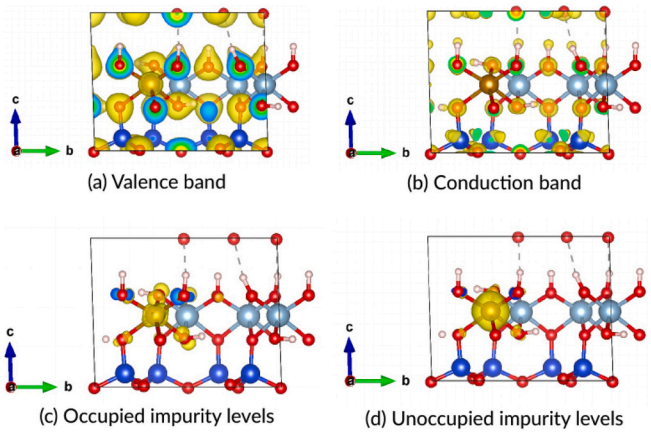

Fig. 4. Charge density ρ in Kaol-Fe2, DFT-D2+U relaxed structure and charge state 0 (U = 4 eV). Isosurfaces are at 0.15 e−/Å^3 in (a) and (b), and 0.02 e−/Å^3 in (c) and (d).

kaolinite (Nisar et al., 2011; Chao et al., 2012; Richard and Rendtorff, 2019; Zhao et al., 2020). In a similar way, in Fig. 4b it can be seen also the significant contribution of the electronic Si levels to the conduction band. On the other hand, Fig. 4c and d allow the inspection of the charge corresponding to the impurity levels presented in the DOS of Fig. 3 (total charge 0 case), and show that such charge is located in the impurity surroundings (Fe atom and its ONNs). In the case of the occupied levels of Fig. 4c (energy range − 3 eV to E_F) it can be seen that the electronic distribution around the Fe impurity atoms is a combination of its 3*d*-orbital projections at the atomic site plus a contribution of the 2*p* orbitals of its oxygen neighbors. The unoccupied levels shown in Fig. 4d (energy range E_F to 1 eV) have these same features. This local distribution of the charge that occupies the impurity levels when one electron is added or subtracted to the system is consistent with the local structural distortions of the octahedral sites discussed above.

3.3. Iron oxidation state assignment and Mössbauer quadrupole splitting

The Hubbard correction has a key role to correctly describe the high-spin oxidation states observed in iron-bearing kaolinites. As mentioned above, when the U value is higher than 2 eV, the magnetization corresponding to the charge states −1 and 0 agrees with those of high-spin Fe^{II} and Fe^{III} ions, respectively, and when U is 0 (which correspond to DFT-D2 method) or lower than 2 eV, the total magnetization of these charge states agrees with those of low-spin iron. In order to show this step-like behavior with more detail, Fig. 5a presents the total magnetization μ as a function of U. As can be seen, for Fe^{II} μ changes from low- to high-spin state when $U = 2$ eV, while for Fe^{III} this happens when $U = 3$ eV.

On the other hand, the GIPAW method allows the calculation of the EFG at the Fe atomic site, from which the Mössbauer QS can be determined. In order to show how the corrections due to the U parameter influence the QS value, in Fig. 5b the predicted QS as a function of U are presented for charge state −1 and 0, using DFT-D2+U and the structure fixed to the $U = 0$ case (*i.e.*, the DFT-D2 relaxed structure). In this figure, they have also indicated the range of experimentally determined QS values for both Fe^{III} and Fe^{II} contributions (St. Pierre et al., 1992; Castelein et al., 2002; Hart et al., 2002; Sei et al., 2004; Scorzelli et al., 2008; Andji et al., 2009; Silva et al., 2009; Murad, 2010; Santos et al., 2012; Gonçalves et al., 2020). In general, Fe^{III} dominates the Mössbauer spectra of most kaolinites, with a temperature-independent QS of about 0.5 mm/s. However, Mössbauer spectra in kaolinites can also show a contribution due to the presence of structural Fe^{II} (contribution up to about 40%), which is characterized by a QS of ~2.5 mm/s at room temperature. As can be seen from Fig. 5b, the U parameter has a strong effect on the predicted QS, and for U values higher than 2 eV it exists a good agreement between the QS predictions and the Mössbauer results. It must be taken into account that the GIPAW results of Fig. 5 correspond to the structure fixed at that obtained with the DFT-D2 method, because its purpose is to show solely how the electronic effects driven by the Hubbard correction modify the QS predictions. In view of this general agreement between DFT-D2+U calculations and the experimental data when $U = 4$ eV and also the good description of Fe local structures using this value for U (as already discussed in the previous section), it can be assigned the charge states 0 and − 1 to the high-spin states of Fe^{III} and Fe^{II} in the iron-bearing kaolinites. Considering this assignment, in Table 2 are summarized the QS predictions before and after structural relaxations with this approach. The results presented in this table weight of the structural distortion effects on the QS predictions. As can be seen, the structural relaxations have minor effects on the predicted QS for both oxidation states. Therefore, the electronic modifications obtained after the Hubbard corrections are the ones that have the major control for the correct description of the experimentally observed QS values.

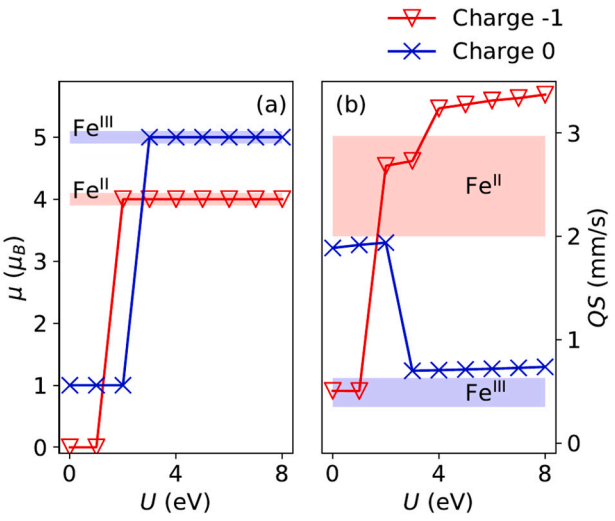

Fig. 5. DFT-D2+U results for (a) total magnetization μ and (b) QS as a function of the U parameter in the Kaol-Fe2 system. The structure is fixed to the $U = 0$ case. In (a) are indicated the nominal magnetization for Fe^{III} and Fe^{II} high-spin oxidation states (5 and 4 μ_B per cell, respectively), and in (b) the range of QS experimental values for both oxidation states are indicated by the colored filled areas.

Finally, a complete table with the calculated values for QS is provided in the supplementary material for further analysis (see Table S4), which includes the EFG values obtained with the DFT, DFT-D2, and DFT-D2+U approaches for the three considered charge states of the Kaol-Fe2 system. Also, a Fig. S6 is included to show the behavior of charge state +1 results for total magnetization and QS as a function of U when the structure is kept fixed. As can be seen in Fig. S6, for this charge state the U parameter also produces a change in the values of the total magnetization and the QS for $U = 4$ eV.

3.4. Discussion

The initial strategy of this work of adding or subtracting an electron to recover the insulator character of the system was similar to the one used in other DFT-based models for iron-bearing clay minerals, where additional defects are included (vacancies or intercalated atoms) (Nisar et al., 2011; Ferreira et al., 2019; Chen et al., 2020). It is common that first principles studies use simplified models of materials, in order to describe some of their properties. Hence, a hypothesis in this work was that in real samples, structural defects can provide the electric charge here included arbitrarily, considering that the purpose of the present investigation was to strictly analyze the Fe-atom environments through the simplified case of structural Fe in an idealized kaolinite bulk structure. In this sense, in this work three charge states were evaluated, which model a kaolinite system with a semiconductor character that ranges from n-type to p-type. Nevertheless, raw clays present a higher complexity due to their multiple structural defects and impurities, which can strongly modify the electronic structure (Pietzsch et al., 2015).

It was shown that Hubbard correction on Fe-3*d* electrons is needed

Table 2
Comparison of QS predictions (expressed in mm/s) using the DFT-D2+U approach ($U = 4$ eV) before and after the structure relaxations. Fe oxidation state assignment is based on the total magnetization analysis. In the last row are included the range of QS experimental values obtained from Mössbauer spectra by other authors (St. Pierre et al., 1992; Castelein et al., 2002; Hart et al., 2002; Sei et al., 2004; Scorzelli et al., 2008; Andji et al., 2009; Silva et al., 2009; Murad, 2010; Santos et al., 2012; Gonçalves et al., 2020).

	Fe^{III}	Fe^{II}
Predicted QS (this work)		
Non-relaxed structure	0.54	2.93
Relaxed structure	0.64	2.86
Experimental QS (from literature)	0.35–0.63	2.00–2.97

for a correct description of many properties of Fe-doped kaolinite simultaneously. Only after the inclusion of a *U* parameter larger than 2 eV is reproduced the insulator character of the compound, the impurity oxidation states, and the local structure and QS at the Fe site. In general, the predicted DOS are in agreement with the background of recent investigations in kaolinite using different first principles calculation methods (He et al., 2009; Nisar et al., 2011; Pietzsch et al., 2015; Fu and Yang, 2017; Richard and Rendtorff, 2019; Zhao et al., 2020). Also, the inclusion of the *U* parameter was recently tested for other Fe-bearing clay minerals such as smectites and montmorillonites (Geatches et al., 2013; Kéri et al., 2017, 2020). In this work it was shown that the *U* correction changes the electronic band gap in the Fe-doped kaolinite, and also can modify the total magnetization of the system. These effects were used to select values of *U* to describe Fe^{III} and Fe^{II} forms, considering an ionic picture for the system in which Fe^{III} is expected to assume a $3d^5$ configuration, and Fe^{II} is expected to assume a $3d^6$ configuration, both in the high-spin state, and in agreement with the experimental observations in kaolins (Murad, 2010). Furthermore, the assignment of the different calculation approaches to Fe^{III} and Fe^{II} based on total magnetization calculations is similar to those recently used by other authors for Fe doped montmorillonite (Ferreira et al., 2019). In this sense, in this work it was shown how for both oxidation states the *U* correction can switch from low-spin to high-spin states. This "switching effect" is also accompanied by a change in the distances from Fe to their oxygen neighbors, producing an Fe local environment with bond lengths in a better agreement with those expected according to the sum of Fe and O atomic radii. On the other hand, following the same charge state assignment, the initially proposed charge state +1 may correspond to a hypervalent Fe^{IV} or, in terms of the system modeling, to a simplified model that represents the case of a high amount of acceptor impurities in the Fe-doped kaolinite system (experimentally non observed).

Compared to the Fe-doped kaolinite relaxed structures obtained with DFT, the addition of the dispersion (D2) correction produces minor changes in what refers to the Fe surroundings (as summarized in Tables S1 and S2). Nevertheless, it must be mentioned that the DFT-D2 relaxed structures present some differences compared to the DFT ones in the OH layer outer surface, which were not explored in detail in this work but it can be seen in Fig. S5. As mentioned, these modifications in the interlayer obtained with D2 practically do not affect the Fe environments, but may be important for describing many processes in phyllosilicates, as other authors warn (Tunega et al., 2012; Cutini et al., 2020).

In regard to the predictions of QS at the Fe sites, this is the first time the GIPAW method is applied to this purpose in an iron-bearing clay mineral. The QS values for high-spin Fe^{III} and Fe^{II} calculated with the DFT-D2+*U* approach are in very good agreement with the experimental results reported in the literature. Therefore, DFT+*U* is an effective approach that can be used as an alternative to DFT-based methods that made use of hybrid functionals to predict hyperfine parameters at Fe atoms (Pápai and Vankó, 2013).

Although the experimental QS values for both contributions are known to be very different (about 0.5 mm/s and 2.5 mm/s), in Table 2 were presented the whole range of reported values. This allows visualizing the effects of real kaolinite structural disorder (vacancies, impurities, *etc.*) on the QS. As shown, the proposed simplified model for the Fe-doped kaolinite, in which idealized pristine kaolinite only has one substitutional Fe atom as a structural defect, adequately describes a much more complex system such as the raw kaolins studied by Mössbauer spectroscopy. This is a consequence of the extremely local character of this hyperfine technique, in which the QS quantity is practically determined by the Fe atom and its direct neighbors. In this sense, in Mössbauer experiments, it is common to broke down the QS into two contributions: the one from the asymmetric distribution of the Fe valence electrons, and the lattice contribution from the neighbor atoms (Murad, 2010). In general, the valence contributions are larger than the lattice contributions, but the half-filled 3*d* shell with five unpaired electrons in Fe^{III} has a near-spherical valence electron distribution, which leads to a relatively low QS (of about 0.5 mm/s). In contrast, high-spin Fe^{II} has a large QS valence contribution from the 6th *d* electron. This behavior for the QS is clearly reflected in Fig. 5b using GIPAW calculations.

In summary, in this work it has been proven that through the DFT-D2+*U* approach many properties of Fe-doped kaolinite can be correctly described, analyzed, and related to the presence of the different forms of structural Fe into the kaolinite host.

4. Conclusions

A detailed analysis of the structural Fe local environments in kaolinites, their oxidation states, and Mössbauer QS were performed with different DFT-based approaches and considering a simple Fe-doped kaolinite model. Grimme's D2 dispersion and Hubbard corrections were assessed using the GIPAW calculation method. It was shown that the different properties at Fe impurity sites can be correctly described using DFT-D2+*U*. As the QS is a quantity highly sensitive to the local environments, the very good accuracy in its prediction contributes to better understand the origin of the measured QS in naturally-occurring kaolins, and supports the GIPAW method for the description of the structural and electronic properties in other iron-containing clay minerals. The obtained results encourage further studies on more complex Fe-doped systems, where typical experiments present difficulties, such as other iron-bearing clay minerals or MK. Some of these investigations are now in progress.

Declaration of Competing Interest

The authors declare that they have no known competing financial interests or personal relationships that could have appeared to influence the work reported in this paper.

Acknowledgments

This work has been supported by the Argentinian funding institutions Consejo Nacional de Investigaciones Científicas y Técnicas (CONICET), Agencia Nacional de Promoción Científica y Tecnológica (ANPCyT, PICT 2016-1193), and Universidad Nacional de La Plata (UNLP, X-904). Part of the results presented in this work have been obtained by using the facilities of the CCT-Rosario Computational Center, member of the High Performance Computing National System (SNCAD, MinCyT-Argentina). The authors are members of CONICET, Argentina.

Appendix A. Supplementary data

Supplementary data to this article can be found online at https://doi.org/10.1016/j.clay.2021.106251.

References

Andji, J.Y.Y., Abba Toure, A., Kra, G., Jumas, J.C., Yvon, J., Blanchart, P., 2009. Iron role on mechanical properties of ceramics with clays from Ivory Coast. Ceram. Int. 35, 571. https://doi.org/10.1016/j.ceramint.2008.01.007.

Andrini, L., Gauna, M.R., Conconi, M.S., Suarez, G., Requejo, F.G., Aglietti, E.F., Rendtorff, N.M., 2016. Extended and local structural description of a kaolinitic clay, its fired ceramics and intermediates: an XRD and XANES analysis. Appl. Clay Sci. 124-125, 39. https://doi.org/10.1016/j.clay.2016.01.049.

Apaolaza, A., Richard, D., Tejerina, M.R., 2020. Experimental and ab initio study of the structural and optical properties of ZnO coatings: Performance of the DFT+U approach. Processing and Application of Ceramics 14 (4), 362–371. https://doi.org/10.2298/PAC2004362A.

Bochevarov, A.D., Friesner, R.A., Lippard, S.J., 2010. Prediction of 57Fe Mössbauer Parameters by Density Functional Theory: a benchmark Study. J. Chem. Theory Comput. 6, 3735. https://doi.org/10.1021/ct100398m.

Castelein, O., Aldon, L., Olivier-Fourcade, J., Jumas, J.C., Bonnet, J.P., Blanchart, P., 2002. 57Fe Mössbauer study of iron distribution in a kaolin raw material: influence

of the temperature and the heating rate. J. Eur. Ceram. Soc. 22, 1767. https://doi.org/10.1016/S0955-2219(01)00496-4.
Chakraborty, A.K., 2014. Phase Transformation of Kaolinite Clay. Springer. https://doi.org/10.1007/978-81-322-1154-9.
Chao, H.M., Jian, Z., Jie, F.Z., 2012. First-principles study of atomic and electronic structures of kaolinite in soft rock. Chin. Phys. B 21, 039101. https://doi.org/10.1088/1674-1056/21/3/039101.
Charpentier, T., 2011. The PAW/GIPAW approach for computing NMR parameters: a new dimension added to NMR study of solids. Solid State Nucl. Magn. Reson. 40, 1–20. https://doi.org/10.1016/j.ssnmr.2011.04.006.
Chen, J., Min, F., Liu, L., Cai, C., 2020. Systematic exploration of the interactions between Fe-doped kaolinite and coal based on DFT calculations. Fuel 266, 117082. https://doi.org/10.1016/j.fuel.2020.117082.
Conconi, M.S., Morosi, M., Maggi, J., Zalba, P.E., Cravero, F., Rendtorff, N.M., 2019. Thermal behavior (TG-DTA-TMA), sintering and properties of a kaolinitic clay from Buenos Aires Province, Argentina. Cerâmica 65, 227. https://doi.org/10.1590/0366-69132019653742621.
Cutini, M., Maschio, L., Ugliengo, P., 2020. Exfoliation Energy of Layered Materials by DFT-D: beware of Dispersion! J. Chem. Theory Comput. 16, 5244–5252. https://doi.org/10.1021/acs.jctc.0c00149.
Danner, T., Norden, G., Justnes, H., 2018. Characterisation of calcined raw clays suitable as supplementary cementitious materials. Appl. Clay Sci. 162, 391. https://doi.org/10.1016/j.clay.2018.06.030.
Daou, I., Lecomte-Nana, G.L., Tessier-Doyen, N., Peyratout, C., Gonon, M.F., Guinebretiere, R., 2020. Probing the dehydroxylation of kaolinite and halloysite by in situ high temperature X-ray diffraction. Minerals 10, 480. https://doi.org/10.3390/min10050480.
Drits, V.A., Derkowski, A., Sakharov, B.A., Zviagina, B.B., 2016. Experimental evidence of the formation of intermediate phases during transition of kaolinite into metakaolinite. Am. Mineral. 101, 2331. https://doi.org/10.2138/am-2016-5776.
Drits, V.A., Sakharov, B.A., Dorzhieva, O.V., Zviagina, B.B., Lindgreen, H., 2019. Determination of the phase composition of partially dehydroxylated kaolinites by modelling their X-ray diffraction patterns. Clay Miner. 54, 309. https://doi.org/10.1180/clm.2019.39.
Fabbri, B., Gualtieri, S., Leonardi, C., 2013. Modifications induced by the thermal treatment of kaolin and determination of reactivity of metakaolin. Appl. Clay Sci. 73, 2. https://doi.org/10.1016/j.clay.2012.09.019.
Ferreira, C.R., Pulcinelli, S.H., Scolfaro, L., Borges, P.D., 2019. Structural and electronic properties of iron-doped sodium montmorillonite clays: a first-principles DFT study. ACS Omega 4, 14369. https://doi.org/10.1021/acsomega.9b00685.
Fu, L., Yang, H., 2017. Structure and electronic properties of transition metal doped kaolinite nanoclay. Nanoscale Res. Lett. 12, 411. https://doi.org/10.1186/s11671-017-2188-4.
Gadikota, G., Zhang, F., Allen, A., 2017. In situ angstrom-to-micrometer characterization of the structural and microstructural changes in kaolinite on heating using Ultrasmall-Angle, Small-Angle, and Wide-Angle X-ray Scattering (USAXS/SAXS/WAXS). Ind. Eng. Chem. Res. 56, 11791. https://doi.org/10.1021/acs.iecr.7b02810.
Gasparini, E., Tarantino, S.C., Ghigna, P., Riccardi, M.P., Cedillo-González, E.I., Siligardi, C., Zema, M., 2013. Thermal dehydroxylation of kaolinite under isothermal conditions. Appl. Clay Sci. 80-81, 417. https://doi.org/10.1016/j.clay.2013.07.017.
Geatches, D.L., Clark, S.J., Greenwell, H.C., 2013. DFT+U investigation of the catalytic properties of ferruginous clay. Am. Mineral. 98, 132–140. https://doi.org/10.2138/am.2013.4204.
Giannozzi, P., Andreussi, O., Brumme, T., Bunau, O., Buongiorno Nardelli, M., Calandra, M., Car, R., Cavazzoni, C., Ceresoli, D., Cococcioni, M., Colonna, N., Carnimeo, I., Dal Corso, A., De Gironcoli, S., Delugas, P., DiStasio Jr., R.A., Ferretti, A., Floris, A., Fratesi, G., Fugallo, G., Gebauer, R., Gerstmann, U., Giustino, F., Gorni, T., Jia, J., Kawamura, M., Ko, H.-Y., Kokalj, A., Kucukbenli, E., Lazzeri, M., Marsili, M., Marzari, N., Mauri, N., Nguyen, N.L., Nguyen, H.-V., Otero-de-la-Roza, A., Paulatto, L., Poncé, S., Rocca, D., Sabatini, R., Santra, B., Schlipf, M., Seitsonen, A.P., Smogunov, A., Timrov, I., Thonhauser, T., Umari, P., Vast, N., Wu, W., Baroni, S., 2017. Advanced capabilities for materials modelling with Quantum ESPRESSO. J. Phys. Condens. Matter 29, 465901. https://doi.org/10.1088/1361-648X/aa8f79.
Gonçalves, M.V.B., Cardoso, A.V., Parreira, F.V., 2020. Intercalation experiments for morphological alteration of kaolinite present in iron ore tailings. Cerâmica 66, 93–105. https://doi.org/10.1590/0366-69132020663782856.
Gualtieri, A.F., Moen, A., Nicholson, D.G., 2000. XANES study of the local environment of iron in natural kaolinites. Eur. J. Mineral. 12, 17–23. https://doi.org/10.1127/0935-1221/2000/0012-0017.
Hart, R.D., St Pierre, T.G., Gilkes, R.J., McKinley, A.J., Siradz, S., Singh, B., 2002. Iron in soil kaolins from Indonesia and Western Australia. Clay Miner. 37, 671. https://doi.org/10.1180/0009855023740069.
He, M.C., Fang, Z.J., Zhang, P., 2009. Theoretical studies on defects of kaolinite in clays. Chin. Phys. Lett. 26, 059101 https://doi.org/10.1088/0256-307X/26/5/059101.
Johnson, E.R., Otero-de-la-Roza, A., 2012. Adsorption of Organic Molecules on Kaolinite from the Exchange-Hole Dipole Moment Dispersion Model. J. Chem. Theory Comput. 8, 5124. https://doi.org/10.1021/ct3006375.
Kéri, A., Dähn, R., Krack, M., Churakov, S.V., 2017. Combined XAFS Spectroscopy and ab initio study on the characterization of iron incorporation by montmorillonite. Environ. Sci. Technol. 51, 10585. https://doi.org/10.1021/acs.est.7b01670.
Kéri, A., Dahn, R., Marques Fernandes, M., Scheinost, A.C., Krack, M., Churakov, S.V., 2020. Iron adsorption on clays inferred from atomistic simulations and XAS studies. Environ. Sci. Technol. 54, 11886–11893. https://doi.org/10.1021/acs.est.9b07962.
Ketkaew, R., Tantirungrotechai, Y., Harding, D.J., Harding, P., Marchivie, M., 2019. OctaDist: A tool for calculating distortion parameters in coordination complexes. https://octadist.github.io.
Kloprogge, J., 2019. Spectroscopic Methods in the Study of Kaolin Minerals and their Modifications. Springer, Springer Mineralogy.
Latta, D.E., Neumann, A., Premaratne, W.A.P.J., Scherer, M.M., 2017. Fe(II)-Fe(III) electron transfer in a clay mineral with low Fe content. ACS Earth Space Chem. 1, 197–208. https://doi.org/10.1021/acsearthspacechem.7b00013.
Lin, X., Ideta, K., Miyawaki, J., Wang, Y., Mochida, I., Yoon, S.-H., 2013. MAS, STMAS and DQMAS NMR studies of the thermal transformation of kaolinite. Appl. Magn. Reson. 44, 1081. https://doi.org/10.1007/s00723-013-0466-6.
Mercier, P.H.J., Le Page, Y., 2008. Kaolin polytypes revisited ab initio. Acta Crystallogr. B 64, 131143. https://doi.org/10.1107/S0108768108001924.
Mudarra Navarro, A.M., Rodríguez Torres, C.E., Errico, L., Nomura, K., 2021. The role of impurities and oxygen vacancies in the magnetic response of FexCoySn1-x-yO2. Experimental and ab initio study. Mater. Chem. Phys. 257, 123822. https://doi.org/10.1016/j.matchemphys.2020.123822.
Murad, E., 1998. Clays and clay minerals: what can Mössbauer spectroscopy do to help understand them? Hyperfine Interact. 117, 39–70. https://doi.org/10.1023/A:1012635124874.
Murad, E., 2010. Mössbauer spectroscopy of clays, soils and their mineral constituents. Clay Miner. 45, 413. https://doi.org/10.1180/claymin.2010.045.4.413.
Nisar, J., Århammar, C., Jämstorp, E., Ahuja, R., 2011. Optical gap and native point defects in kaolinite studied by the GGA-PBE, HSE functional, and GW approaches. Phys. Rev.B 84, 075120. https://doi.org/10.1103/PhysRevB.84.075120.
Pápai, M., Vankó, G., 2013. On predicting Mössbauer parameters of Iron-containing molecules with Density-Functional Theory. J. Chem. Theory Comput. 9, 5004. https://doi.org/10.1021/ct4007585.
Paris, M., 2014. The two aluminum sites in the 27Al MAS NMR spectrum of kaolinite: Accurate determination of isotropic chemical shifts and quadrupolar interaction parameters. Am. Mineral. 99, 393. https://doi.org/10.2138/am.2014.4607.
Petit, S., Decarreau, A., 1990. Hydrothermal (200°C) synthesis and crystal chemistry of iron-rich kaolinites. Clay Miner. 25, 181. https://doi.org/10.1180/claymin.1990.025.2.04.
Pickard, C.J., Mauri, F., 2001. All-electron magnetic response with pseudopotentials: NMR chemical shifts. Phys. Rev. B 63, 245101. https://doi.org/10.1103/PhysRevB.63.245101.
Pietzsch, A., Nisar, J., Jämstorp, E., Gråsjö, J., Århammar, C., Ahuja, R., Rubensson, J.E., 2015. Kaolinite: defect defined material properties - a soft X-ray and first principles study of the band gap. J. Electron Spectros. Relat. Phenomena 202, 11. https://doi.org/10.1016/j.elspec.2015.02.003.
Profeta, M., Mauri, F., Pickard, C.J., 2003. Accurate first principles prediction of 17O NMR parameters in SiO2: assignment of the zeolite ferrierite spectrum. J. Am. Chem. Soc. 125, 541. https://doi.org/10.1021/ja027124r.
Provis, J.L., Yong, S.L., Duxson, P., 2009. Nanostructure/microstructure of metakaolin geopolymers. Geopolymers 72. https://doi.org/10.1533/9781845696382.1.72.
Richard, D., Gil Rebaza, A.V., 2020. The GIPAW approach for the study of local structures and the electric field gradients at Cd and Ta impurity sites. Application to doped yttria ceramics. Comput. Mater. Sci. 171, 109224. https://doi.org/10.1016/j.commatsci.2019.109224.
Richard, D., Rendtorff, N.M., 2019. First principles study of structural properties and electric field gradients in kaolinite. Appl. Clay Sci. 169, 67. https://doi.org/10.1016/j.clay.2018.12.013.
Rivard, C., Montargès-Pelletier, E., Vantelon, D., Pelletier, M., Karunakaran, C., Michot, L.J., Villieras, F., Michau, N., 2013. Combination of multi-scale and multi-edge X-ray spectroscopy for investigating the products obtained from the interaction between kaolinite and metallic iron in anoxic conditions at 90 C. Phys. Chem. Minerals 40, 115–132. https://doi.org/10.1007/s00269-012-0552-6.
Rocha-Rodrigues, P., Santos, S.S.M., Miranda, I.P., Oliveira, G.N.P., Correia, J.G., Assali, L.V.C., Petrilli, H.M., Araújo, J.P., Lopes, A.M.L., 2020. Ca3Mn2O7 structural path unraveled by atomic-scale properties: a combined experimental and ab initio study. Phys. Rev. B 101, 064103. https://doi.org/10.1103/PhysRevB.101.064103.
Santos, E., Scorzelli, R.B., Bertolino, L.C., Alves, O.C., Munayco, P., 2012. Characterization of kaolin from the Capim River region -Brazil. Appl. Clay Sci. 55, 164. https://doi.org/10.1016/j.clay.2011.11.009.
Schroeder, P.A., Erickson, G., 2014. Kaolin: from ancient porcelains to nanocomposites. Elements 10, 177–182. https://doi.org/10.2113/gselements.10.3.177.
Scorzelli, R.B., Bertolino, L.C., Luz, A.B., Duttine, M., Silva, F.A.N.G., Munayco, P., 2008. Spectroscopic studies of kaolin from different Brazilian regions. Clay Miner. 43, 129–135. https://doi.org/10.1180/claymin.2008.043.1.03.
Sei, J., Abba Touré, A., Olivier-Fourcade, J., Quiquampoix, H., Staunton, S., Jumas, J.C., Womes, M., 2004. Characterisation of kaolinitic clays from the Ivory Coast: identification of structural Fe. Hyperfine Interact. 155, 51–64. https://doi.org/10.1023/B:HYPE.0000035159.17646.e0.
Shannon, R.D., 1976. Revised effective ionic radii and systematic studies of interatomic distances in halides and chalcogenides. Acta Cryst A32, 751–767. https://doi.org/10.1107/S0567739476001551.
Silva, F.A.N.G., Luz, A.B., Sampaio, J.A., Bertolino, L.C., Scorzelli, R.B., Duttine, M., Teixeira da Silva, F., 2009. Technological characterization of kaolin: Study of the case of the Borborema–Seridó region (Brazil). Appl. Clay Sci. 44, 189. https://doi.org/10.1016/j.clay.2009.01.015.
Smrcok, L., Tunega, D., Ramirez-Cuesta, A.J., Scholtzová, E., 2010. The combined inelastic neutron scattering and solid state DFT study of hydrogen atoms dynamics in a highly ordered kaolinite. Phys. Chem. Minerals 37, 571–579. https://doi.org/10.1007/s00269-010-0358-3.

Soltermann, D., Marques Fernandes, M., Baeyens, B., Dähn, R., Joshi, P.A., Scheinost, A. C., Gorski, C.A., 2013. Fe(II) uptake on natural montmorillonites. I. Macroscopic and spectroscopic characterization. Environ. Sci. Technol. 48, 8688–8697. https://doi.org/10.1021/es501887q.

Soro, N., Aldon, L., Olivier-Fourcade, J., Jumas, J.C., Laval, J.P., Blanchart, P., 2003. Role of iron in mullite formation from kaolins by Mössbauer spectroscopy and Rietveld refinement. J. Am. Ceram. Soc. 86, 129. https://doi.org/10.1111/j.1151-2916.2003.tb03289.x.

St. Pierre, T.G., Singh, B., Webb, J., Gilkes, B., 1992. Mössbuer spectra of soil kaolins from South-Western Australia. Clay Clay Miner. 40, 341. https://doi.org/10.1346/CCMN.1992.0400315.

Tunega, D., Bučko, T., Zaoui, A., 2012. Assessment of ten DFT methods in predicting structures of sheet silicates: Importance of dispersion corrections. J. Chem. Phys. 137, 114105. https://doi.org/10.1063/1.4752196.

Wagner, F.E., Wagner, U., 2004. Mössbauer spectra of clays and ceramics. Hyperfine Interact. 154, 35–82. https://doi.org/10.1023/B:HYPE.0000032113.42496.f2.

White, C.E., Provis, J.L., Riley, D.P., Kearley, G.J., van Deventer, J.S.J., 2009. What is the Structure of Kaolinite? Reconciling Theory and Experiment. J. Phys. Chem. B 113, 6756. https://doi.org/10.1021/jp810448t.

White, C.E., Kearley, G.J., Provis, J.L., Riley, D.P., 2013. Inelastic neutron scattering analysis of the thermal decomposition of kaolinite to metakaolin. Chem. Phys. 427, 82. https://doi.org/10.1016/j.chemphys.2013.08.009.

Yan, Y., Wang, H., 2018. In-situ high temperature X-ray diffraction study of dickite. Appl. Clay Sci. 163, 137. https://doi.org/10.1016/j.clay.2018.07.021.

Zalutskii, A.A., 2014. Investigation of the processes of iron-ion recharging on surfaces of natural nanoclays (based on Mössbauer spectroscopy data). J. Surf. Invest.: X-Ray, Synchrotron Neutron Tech. 6, 51–58. https://doi.org/10.1134/S1027451014030379.

Zhao, J., Qin, X., Wang, J., He, M., 2020. Effect of Mg(II) and Na(I) doping on the electronic structure and mechanical properties of kaolinite. Minerals 10, 368. https://doi.org/10.3390/min10040368.

Zhou, B., Sherriff, B.L., Wang, T., 2009. 27Al NMR spectroscopy at multiple magnetic fields and ab initio quantum modeling for kaolinite. Am. Mineral. 94, 865. https://doi.org/10.2138/am.2009.3142.

Zhu, B.L., Qi, C.L., Zhang, Y.H., Bisson, T., Xu, Z., Fan, Y.J., Sun, Z.X., 2019. Synthesis, characterization and acid-base properties of kaolinite and metal (Fe, Mn, Co) doped kaolinite. Appl. Clay Sci. 179, 105138. https://doi.org/10.1016/j.clay.2019.105138.

Zyabkin, D.V., Gunnlaugsson, H.P., Gonçalves, J.N., Bharuth-Ram, K., Qi, B., Unzueta, I., Naidoo, D., Mantovan, R., Masenda, H., Ólafsson, S., Peters, G., Schell, J., Vetter, U., Dimitrova, A., Krischok, S., Schaaf, P., 2020. Experimental and theoretical study of electronic and hyperfine properties of hydrogenated anatase (TiO2): defect interplay and thermal stability. J. Phys. Chem. C 124, 7511. https://doi.org/10.1021/acs.jpcc.0c00085.